Journal of Global Positioning Systems (2026)
Vol. 22, Issue 1: 90-98
DOI:10.5081/jgps.22.1.90

LiDAR-Inertial-UWB Integrated Localization with Quality Control and Online NLOS Mitigation for Unmanned Ground Vehicles

Hong Liu[1,2], Shuguo Pan[1,2*], Wang Gao[1,2], Jinle Xu[1,2], Zhuoxuan Wang[1,2], Feixuan Huang[1,2]

[1]School of Instrument Science and Engineering, Southeast University, Southeast University, Nanjing, 210096, China.

[2]State Key Laboratory of Comprehensive PNT Network and Equipment Technology, Southeast University, Nanjing, 210096, China.

*Corresponding author(s). E-mail(s): psg@seu.edu.cn;
Contributing authors: hong@seu.edu.cn; gaow@seu.edu.cn; xujinle@seu.edu.cn; wangzhuoxuan@seu.edu.cn; huangfeixuan@seu.edu.cn;

Abstract: Continuous and precise localization constitutes a fundamental prerequisite for intelligent vehicles and autonomous driving, particularly in challenging environments, such as GNSS signal blockage, laser degeneration and vision illumination variations. In this paper, we propose a system that integrates data from light detection and ranging (LiDAR), inertial sensor, and ultrawideband (UWB) to achieve global positioning through filtering and smoothing techniques in diverse scenes. Firstly, we leverage an Extended Kalman Filter (EKF) to handle ranging measurements, while also online distinguishing and removing None Line of Sight (NLOS) errors. Besides, a quality control module is performed to obtain healthy UWB absolute factor in the backend. Secondly, a precise inertial navigation system (INS) mechanization algorithm is employed to achieve state updates, which also contributes to the LiDAR-inertial partly tight-coupled process. Finally, we propose a lightweight factor graph to optimally fuse marginalization factor, relative LiDAR odometry factor, UWB absolute factor and preintegration factor. We conducted extensive experiments in outdoor and NLOS scenarios using a customized platform. The results show that our integrated positioning approach enhances the accuracy of existing state-of-the-art schemes, while also enabling robust and real-time pose estimation for unmanned ground vehicles.

Keywords: Multi-source integration positioning, filter, factor graph optimization, vehicle localization

1 Introduction

Accurate and robust state estimation is a critical cornerstone for the reliable operation of unmanned ground vehicles (UGVs) in complex application scenarios, ranging from industrial inspection and disaster rescue to autonomous patrol and smart agriculture [1]. Among the mainstream positioning solutions, Global Navigation Satellite System (GNSS)-based technologies have been widely used, but their applicability is greatly restricted in scenarios with severe signal blockage, such as urban canyons, dense forests, and underground facilities. To solve this problem, researchers have turned to multi-sensor fusion technologies, integrating inertial measurement units (IMUs), visual sensors, light detection and ranging (LiDAR), Bluetooth modules, and ultrawideband (UWB) devices to compensate for the defects of single-sensor positioning [2][3].

In environments where traditional GNSS systems are unavailable, such as underground mines, using LiDAR, INS, and other relative navigation approaches can result in error accumulation over time. In recent decades, novel global positioning strategies represented by Bluetooth, radio frequency identification devices (RFID), WIFI and UWB are research hotspots [4]. An online machine learning method is proposed, extracting sound patterns and matching localization for Bluetooth devices [5]. In another approach, RFID phase samples can be integrated with odometer data, which improves the capability of localization [6]. WIFI has also been applied in various scenarios without deploying anchor stations, with range information, angle-of-arrival and Doppler shift being fused in the state estimator in [7]. Finally, ultrawideband technology offers high transmission rate, low transmission power, and strong penetration, making it a more robust option for GNSS-denied positioning and navigation compared to other wireless sensors [8].

The fusion of LiDAR and IMU has become a mainstream solution for UGV positioning in GNSS-denied environments, leveraging the complementary advantages of the two sensors [9]. LiDAR provides high-precision spatial measurements and dense 3D point clouds, enabling effective environmental mapping, while IMU offers high-frequency motion state information (including acceleration and angular velocity) to maintain stable pose estimation during short-term LiDAR data loss or featureless scenarios [10][11]. However, LiDAR-IMU fusion systems still suffer from inherent limitations: they rely on recursive positioning principles, leading to gradual accumulation and dispersion of drift errors over long-term operation, especially in large-scale unstructured environments where loop closure opportunities are scarce [12]. To address this long-term drift problem and achieve globally consistent positioning, the integration of an absolute positioning sensor such as UWB is highly necessary, as UWB can provide precise absolute distance measurements to anchor points, which can effectively correct the cumulative errors of LiDAR-IMU fusion systems.

Similarly, the fusion of UWB and IMU has emerged as a promising approach for high-precision positioning in GNSS-denied scenarios, combining the absolute positioning capability of UWB with the high-frequency motion sensing of IMU. IMU can compensate for the intermittent UWB signal and low update rate, providing continuous motion estimation to ensure positioning continuity when UWB signals are blocked or interrupted [13]. Tightly coupled UWB-IMU fusion frameworks based on Extended Kalman Filter (EKF) or factor graph optimization have been proposed to improve positioning accuracy, with None-Line-of-Sight (NLOS) mitigation modules further enhancing system robustness [14, 15]. Nevertheless, UWB-IMU fusion systems have obvious shortcomings: UWB ranging accuracy is easily affected by multipath effects and anchor station layout, especially in environments with dense obstacles. Therefore, integrating LiDAR into the UWB-IMU fusion system is essential, as LiDAR can provide detailed environmental spatial information and map construction, while its high-precision relative positioning capability can compensate the limitations of UWB in dynamic and complex scenarios [16, 17]. To address the above issues, the innovation of our method lies in:

(a) We propose a filtering and smoothing framework to fuse LiDAR, IMU and UWB, which balances both efficiency and accuracy.

(b) NLOS removal and quality control modules are employed for ranging measurement processing. Besides, precise INS mechanization is introduced for state update. And the prior information is applied in partly tight-coupled LiDAR inertial odometry.

(c) We conduct extensive experiments based on an unmanned ground vehicle in diverse scenes to demonstrate the robustness and accuracy of our system. In addition, globally consistent point cloud maps can be obtained.

2 Method

The pipeline of our method is shown in Fig. 1. We employ the extended Kalman filter and factor graph optimization, which incorporate modules for NLOS mitigation and quality control.

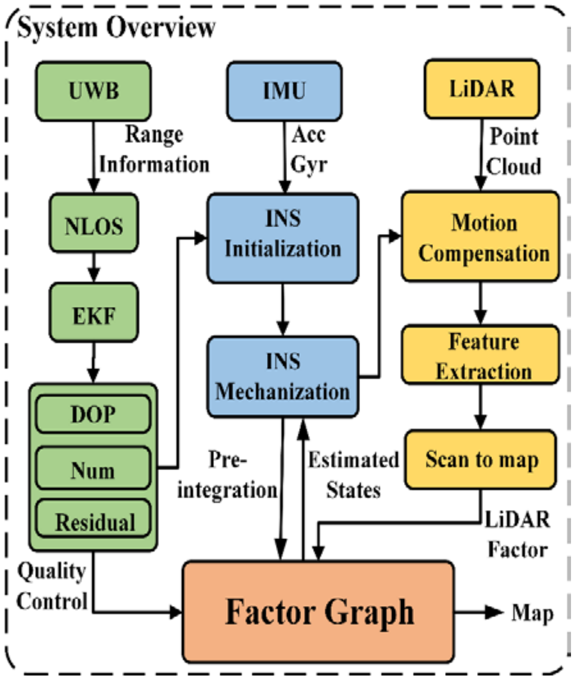

Fig. 1 The pipeline of the proposed system.

2.1 INS Mechanization

In our work, high-precision INS mechanization is deployed for pose estimation. And IMU measurements include instantaneous angular velocity $\tilde{\omega}_b$ and line acceleration $\tilde{\boldsymbol{a}}_b$, which contain some error terms. The mathematical models are expressed as follows:

$$\begin{cases} \tilde{\boldsymbol{\omega}}_b = \boldsymbol{\omega}_b^w + \boldsymbol{b}_g + \boldsymbol{n}_g \\ \tilde{\boldsymbol{a}}_b = \mathbf{R}_b^w(\boldsymbol{a}_b^w - \boldsymbol{g}^w) + \boldsymbol{b}_a + \boldsymbol{n}_a \end{cases} \tag{1}$$

wherein $\boldsymbol{b}_g, \boldsymbol{b}_a$ denote the slowly changing bias vectors, $\boldsymbol{n}_g, \boldsymbol{n}_a$ represent the white noise vectors, and the subscript g and a represent the gyroscopes and accelerometers, respectively, and $\mathbf{R}_b^w$ denotes the rotation matrix of the pose. And the dynamic position, velocity and attitude model in global frame can be expressed as [18]:

$$\dot{\boldsymbol{q}}_{wb} = \frac{1}{2}\boldsymbol{q}_{wb} \otimes \begin{bmatrix} \boldsymbol{0} \\ \omega_b^w \end{bmatrix}_\times \tag{2}$$

$$\dot{\boldsymbol{v}}^w = \mathbf{R}_b^w \boldsymbol{a}_b^w + \boldsymbol{g}^w \tag{3}$$

$$\dot{\boldsymbol{p}}^w = \boldsymbol{v}^w \tag{4}$$

wherein $\boldsymbol{g}^w$ is the gravity vector in global frame. $[\bullet]_\times$ means vectors map to an antisymmetric matrix.

2.2 LiDAR-Inertial Partly Tight-Coupled Process

Prior information of INS is employed to register between the current frame and the local map. High-frequency information of INS is utilized to de-skew for LiDAR scan. Assuming that point p_l in the current scan is at timestamp t and the timestamp of the scan-end is t_k, INS system can obtain the relative pose change between t and t_k, and $\tilde{\omega}_b, \tilde{a}_b$ represent the IMU measurement in the interval $[t, t_k]$. Therefore, $\mathbf{T}_t^{t_k}$ is computed as:

$$\mathbf{T}_t^{t_k} = Exp\left(\int_t^{t_k} \xi(\tilde{\omega}_b, \tilde{a}_b) dt\right) \tag{5}$$

wherein $Exp(\cdot)$ is the exponential mapping on $se(3)$, $\int_t^{t_k} \cdot dt$ represents the propagation process between the current point from the last point over the time interval $\Delta t = t_k - t$ in this process. And the LiDAR points in the scan are all projected to the scan-end frame by

$$p_l^{t_k} = \mathbf{R}_l^b p_l + p_t^{t_k} + p_l^b \tag{6}$$

where $\mathbf{T}_l^b = [\mathbf{R}_l^b, p_l^b]$ represents the extrinsic transform matrix.

Meanwhile, inspired by LOAM [10], the measurement model can be formulated as follow:

$$(p_l^w - p_p)^{\mathrm{T}} n_p = 0 \tag{7}$$

where p_l^w is the point in the world frame, n_p and p_p are the normal vector and point lying on the related plane, respectively. And equation of LiDAR observation is:

$$\hat{z} = z^{å} + \mathbf{J}_x \delta x + \mathbf{J}_n n_l \tag{8}$$

where n_l represents the observation noise vector. The superscript å represents the true value without noise. δx and n_l denote the estimation error and LiDAR point measurement error vectors, while $\mathbf{J}_x$ is the Jacobian matrix of the current state vector and $\mathbf{J}_n$ is the Jacobian matrix of the noise vector. The formula (8) is composed of three terms. It should be noted that the first term is equivalent to zero, the second term is about the state (i.e. $\mathbf{J}_x \delta x$), and the third term implies $\mathbf{J}_n n_l$. Partly tight-coupled LiDAR-inertial odometry takes advantage of the prior information of inertial navigation and LiDAR point cloud measurements. The iterative equation is as follow:

$$\delta x = -(\mathbf{J}_x^{\mathrm{T}} \mathbf{J}_x)^{-1} \mathbf{J}_x^{\mathrm{T}} \hat{z} \tag{9}$$

2.3 UWB Measurement Model and Quality Control

We adopt an EKF solution to deal with the range information. In this part, the UWB state is written as

$$x_u = [p_u^w, v_u^w]^{\mathrm{T}} \tag{10}$$

where p_u^w, v_u^w denote the UWB position and velocity in the global frame. $x_u(k)$ and $x_u(k-1)$ denote two consecutive measurements. The state forward propagation equation is modeled as

$$\hat{x}_u(k \mid k-1) = \mathbf{F}\hat{x}_u(k-1) \tag{10}$$

with the propagation covariance as follow:

$$\mathbf{P}_u(k \mid k-1) = \mathbf{F}\mathbf{P}_u(k-1)\mathbf{F}^{\mathrm{T}} + \mathbf{Q} \tag{11}$$

The updated estimation and covariance are acquired by fusing last ranging measurements, which is associated with process noise $\mathbf{Q}$. And $\mathbf{P}_u$ is the covariance. In this process, the assumption of constant velocity is applied for the EKF, so we can derive the matrix $\mathbf{F}$:

$$\mathbf{F} = \begin{bmatrix} \mathbf{I}_{3\times3} & \Delta \mathrm{T} \mathbf{I}_{3\times3} \\ \mathbf{0}_{3\times3} & \mathbf{I}_{3\times3} \end{bmatrix} \tag{12}$$

where $\Delta \mathrm{T}$ and $\mathbf{I}_{3\times3}$ represent the sampling interval and identity matrix with three rows and three columns.

$$d_i = \| p_u^w - p_{a,i}^w \| + n_d \tag{13}$$

where $\| p_u^w - p_{a,i}^w \|$ represents the true value of distance. n_d is the gaussian white noise. The observation vector is denoted as $z_u = [d_1, d_2, \ldots, d_m]^{\mathrm{T}}$, where m is the number of UWB ranging measurements. Therefore, we can get the measurement model

$$z_u = h(x_u) + n_u \tag{14}$$

And the Jacobian matrix is:

$$\mathbf{H} = \frac{\partial h(x_u)}{\partial p_u^w} \tag{15}$$

Before update process, the propagated state $\hat{x}_u(k \mid k-1)$ and observation vector z_u may include the NLOS or multipath error. We employ two tactics as below.

2.3.1 NLOS Judgment and Removal

In our work, we aim to explore the EKF potential and the criteria is introduced by EKF residual, which is defined as:

$$r = z_u - h(\hat{x}_u(k \mid k-1)) \tag{16}$$

The UWB propagation and ranging measurement must have small differences nearly in line-of-sight environment. Thus, we adjust the Kalman gain $\mathbf{K}'$ according to the residual value as:

$$\mathbf{K}' = \begin{cases} \mathbf{K}, & \|r\| < \gamma_1 \\ 0, & \|r\| \geq \gamma_1 \end{cases} \tag{17}$$

where the threshold γ_1 is empirical value (set to 0.35).

Combining the predicted state and measurements, we obtain the update state for x_u:

$$\hat{x}_u(k) = \hat{x}_u(k \mid k-1) + \mathbf{K}' r \tag{18}$$

with the update covariance:

$$\mathbf{P}_u(k) = (\mathbf{I} - \mathbf{K}'\mathbf{H})\mathbf{P}_u(k \mid k-1) \tag{19}$$

2.3.2 Quality Control

Dilution of precision (DOP) is originally used in the field of satellite navigation, which reflect the influence of satellite distribution on positioning. Inspired by this, the calculation of UWB DOP is:

$$\mathbf{DOP} = \sqrt{tr\left((\mathbf{H}^{\mathrm{T}}\mathbf{H})^{-1}\right)} \tag{20}$$

where $\sqrt{tr(\bullet)}$ represents the trace operation.

When the DOP value is the smallest, the geometric layout of the anchor station corresponding to the tag node is optimal. Therefore, when the layout of UWB anchor nodes is poor, it can be discarded according to the value of DOP (the value is set to 3.0). Additionally, the number of anchor station and the average residual are also important metrics. If there are less than 4 anchor stations, the UWB positioning results are not accurate enough. Moreover, after the NLOS error is removed, it can be concluded that the UWB positioning is effective when average residual is less than the threshold value (set to 0.15).

2.4 Global Optimization Model

In order to reduce the cumulative error, we construct a lightweight factor graph model shown in Fig. 2, which integrates LiDAR odometry constraint, UWB absolute observation and IMU pre-integration as follows:

1) The LiDAR odometry factor is composed of the relative transformation so as to reduce computational cost. And the residual is defined as:

$$r_{LO}(i,j) = \left\| {}^{\hat{x}_j}_{\hat{x}_i}\mathbf{T} \oplus ({}^{x_j^{LO}}_{x_i^{LO}}\mathbf{T})^{\wedge} \right\| \tag{21}$$

2) IMU pre-integration is widespread in navigation due to its function and efficiency. In our work, we also add it in the factor graph. The residual of pre-integration factor can be expressed as:

$$\boldsymbol{r}_{IMU}(\boldsymbol{i},\boldsymbol{j}) = \begin{bmatrix} \boldsymbol{q}_{wj}^{-1} \otimes \boldsymbol{q}_{wi} \otimes \alpha_{ij} \\ \boldsymbol{v}_j - \boldsymbol{v}_i - \boldsymbol{g}^w \Delta \boldsymbol{t}_{ij} - \mathbf{R}_w^i \beta_{ij} \\ \boldsymbol{p}_j - \boldsymbol{p}_i - \boldsymbol{v}_i \Delta \boldsymbol{t}_{ij} - \frac{1}{2}\boldsymbol{g}^w \Delta \boldsymbol{t}_{ij}^2 - \mathbf{R}_w^i \gamma_{ij} \end{bmatrix} \tag{22}$$

where Δt_{ij} represents the time interval between two scans. $\boldsymbol{q}_{wi}, \boldsymbol{p}_i, \boldsymbol{v}_i$, and $\boldsymbol{q}_{wj}, \boldsymbol{p}_j, \boldsymbol{v}_j$ are the key-frame estimated rotation, translation and velocity. $\alpha_{ij}, \beta_{ij}, \gamma_{ij}$ represent position, velocity and attitude between two relative frames. Therefore, the joint equation is:

$$r_{total} = \sum_{i,j} r_{LO}(i,j) + \sum_{i,j} r_{IMU}(i,j) + \sum_{k} r_{UWB}(k) + r_{prior} \tag{23}$$

the optimal states can be optimized according to (24). It is noted that r_{prior} is the prior factor, which is the marginalized state beyond the sliding window. r_{UWB} is the UWB odometry estimation residual. When the motion translation is greater than 1m, or the change posture is greater than 0.5 degrees, the factor graph optimization is performed.

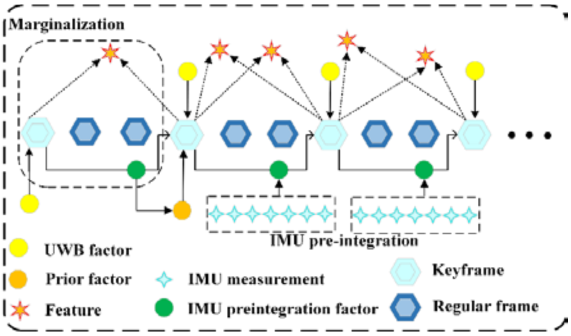

Fig. 2. The structure of the factor graph.

3 Experiments

3.1 Sensor Setup

As shown in Fig. 3, the experimental mobile platform is equipped with a MEMS-based inertial navigation system (ADIS16497), a UWB module, and a Velodyne 16-channel LiDAR. The detailed parameters are shown in Table 1. The dedicated satellite antenna is adopted to receive and capture satellite navigation signals. For trajectory validation, the ground truth is obtained through post-mission forward and backward solution calculations using Inertial Explorer software. We implement the algorithm in Ubuntu with the ROS platform.

Fig. 3 The UGV platform with sensors.

Table 1 Key Parameters of Sensors

	Model	Characteristics
IMU	ADIS16497	6-axis MEMS output frequency: 100 Hz
UWB	Nooploop LinkTrack P-B	ranging accuracy: 5 cm output frequency: 50 Hz maximum communication distance: over 150 m
LiDAR	Velodyne	16-line LiDAR, ranging accuracy: 2 cm, maximum detection

range: 100 m

3.2 Accuracy Evaluation

Exhaustive evaluations are conducted in this section. We use LIO-SAM [12], FAST-LIO2 [9], and LiLi-OM [19] as comparative methods. Meanwhile, we also adopt the loop closure in LIO-SAM for benchmark comparison. We implement Root Mean Square Error (RMSE) and Maximum (MAX) evaluation for absolute translational error. These are important indicators for subsequent planning and control towards UGVs. We conduct experiments across three campus scenarios, namely Scene 1, Scene 2 and Scene 3. Scene 1 involves a trajectory with frequent sharp turns. Scene 2 is captured in an open space crowded with abundant dynamic objects that cause localization interference. Scene 3 consists of a smooth straight path on flat terrain under simple environmental conditions.

The results are shown in Table 2. As can be seen, our LiDAR/IMU odometry has the best performance compared with other LiDAR-inertial SLAM benchmarks, including LIO-SAM (without loop closure module), LiLi-OM and FAST-LIO2. This is because the INS mechanization and tightly-coupled LiDAR-inertial process can improve the accuracy of inertial navigation solution and promote the efficiency of scan-to-map module. In Scene 1, the moving trajectory is easy for loop closure detection, which is conducive to suppressing error. From Table 1, when the loop closure algorithm is applied, the precision of the LIO-SAM algorithm is comparable to that of our integration scheme. And the maximum error is slightly lower than that of our system in Scene 1. In practical application, loop closure is not always happening, hence the straight-line motion in Scene 2 is introduced for experimental verification. It should be noted that our system shows better performance than LIO-SAM with loop closure and other benchmarks. Finally, the dynamic objects in Scene 3 bring fewer stable features, leading to incorrect matching.

Due to the UWB involvement, the accuracy of all sequences has been promoted, showing the improvements of (26.2%, 16.3%, 44.2%) compared to LiDAR/IMU integration in three scenes respectively. Scene 3 is chosen for our analysis. The trajectory is presented in Fig. 4. The blue rectangle includes the dynamic objects and sharp turn motion, bringing certain error in the comparison. Apart from that, the rest of the trajectory is consistent with the ground truth. Moreover, the three-dimensional position error in ECEF is shown in Fig. 5.

Table 2 PERFORMANCE COMPARISON IN THREE SCENES

RMSE(m) /MAX(m)	**Scene 1**	**Scene 2**	**Scene 3**
LIO-SAM (w/o loop)	0.434 /0.768	0.586 /1.828	1.521 /3.281
LIO-SAM (w/ loop)	0.220 **/0.520**	0.365 /0.867	0.582 /1.893
LiLi-OM	2.473 /4.779	0.788 /1.558	4.220 /14.528
FAST-LIO2	0.271 /0.617	1.027 /2.312	1.258 /2.220
LiDAR/IMU	0.279 /0.602	0.264 /0.720	0.491 /2.101
LIU-fusion	**0.206** /0.585	**0.221** **/0.660**	**0.274** **/0.693**

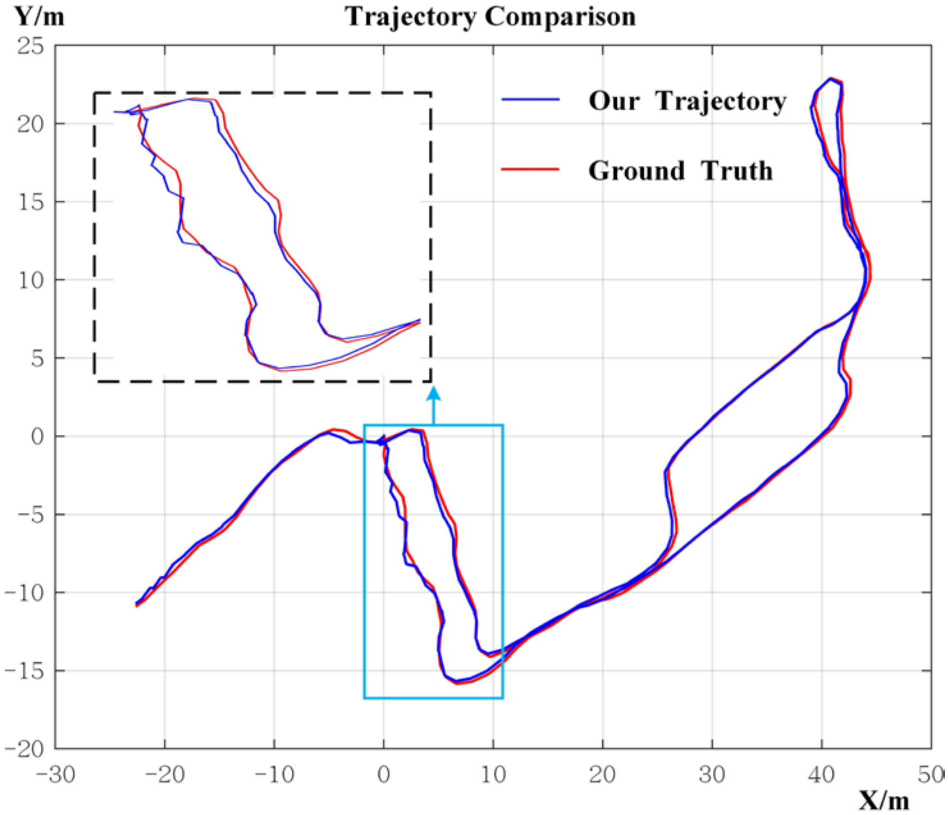

Fig. 4 Trajectory in scene 3. Blue rectangle represents the trajectory in the beginning.

The blue rectangle denotes the larger error in the beginning. The ranging constraints from anchor stations further enhance the accuracy and reliability, which is beneficial for correcting drift and obtain globally consistent trajectory and map in Fig. 6. The point cloud map of Scene 3 corresponds to the real-world scenario. From the photo labeled with letters, we can clearly see the objects such as cars, bus and traffic cones.

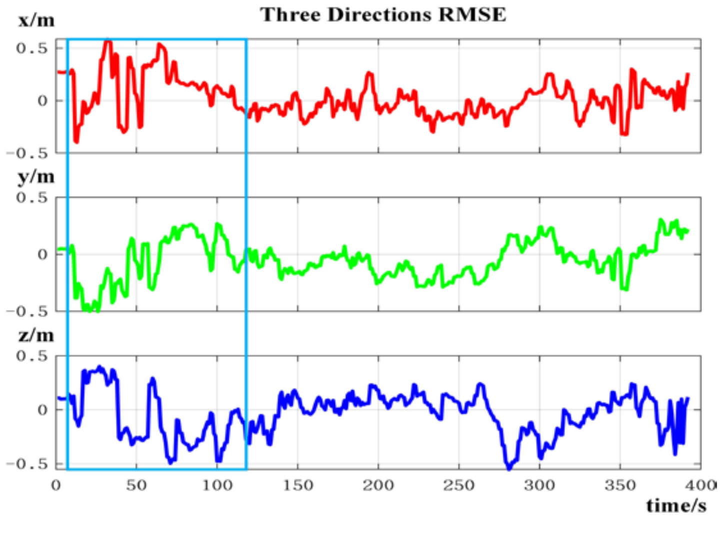

Fig. 5 The three-dimensional position error in ECEF

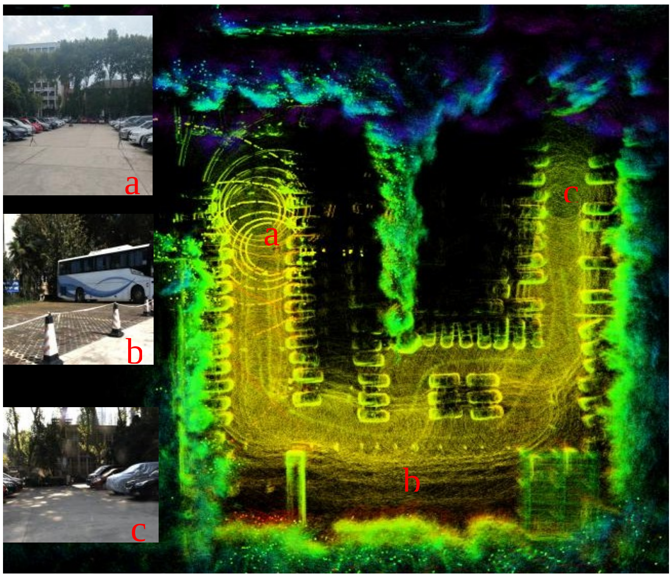

Fig. 6 Mapping result of Scene 3. And the point cloud is colored by height.

3.3 UWB Multipath and NLOS Scene

We deploy four anchor stations in the experiment Most UWB signals are blocked by thick trees shown in Fig. 7. A large number of tree trunks, dense branches and leaves form complex occlusion barriers, which severely block and attenuate most transmitted UWB signals. Unlike open and unobstructed scenarios, the dense forest environment causes non-line-of-sight propagation of UWB signals in most detection areas. The widespread signal occlusion not only weakens the received signal strength but also easily induces multipath interference and signal delay errors, which brings great challenges to high-precision UWB localization and fully simulates the complex and variable actual working conditions of outdoor positioning systems. We implement the experiment where the vehicle runs in the occlusion area for 90 seconds, during which it only receives direct signal from two anchor stations. We would like to clarify that UWB-only and UWB/INS-only solutions diverge in our test scenarios due to prolonged NLOS occlusion, and therefore cannot yield stable quantitative results for comparison. Results are listed in Table 3. The uneven road in this test leads to the failure of LiLi-OM system, and other benchmarks have the similar influence. INS mechanization prior information and the partially tight-coupled method contribute to the lower RMSE in LiDAR/IMU integration compared with LIO-SAM (w/o loop) and FAST-LIO2. Owing to the quality control module, several outliers are excluded. Meanwhile, effective UWB ranging information is beneficial to state estimation, which ensure reliable and low-drift positioning. We can conclude from the Table 3 that our system is more robust and has the highest accuracy. Compared with LiDAR/IMU integration, our system shows the improvements of 57.1% and 19.1% in RMSE and MAX, respectively.

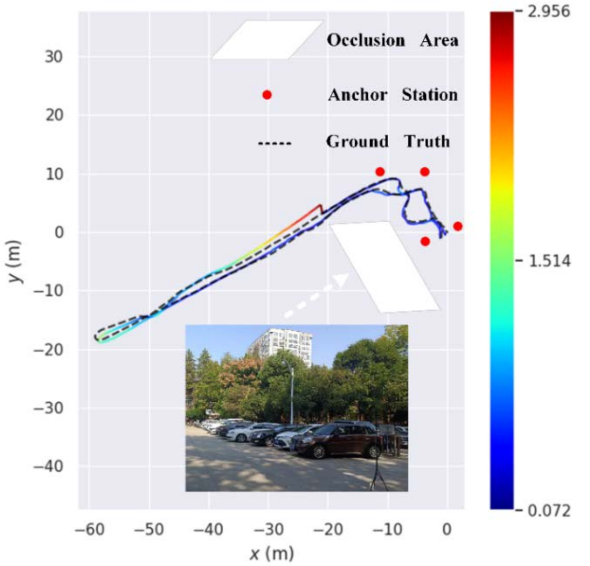

Fig. 7 Trajectory with error color-bar in NLOS scene. The white parallelogram is the occlusion area with thick trees.

Table 3 RMSE IN NLOS SCENE

	RMSE(m) /MAX(m)
LIO-SAM (w/o loop)	1.693/4.431
LIO-SAM (w/ loop)	1.19/3.009
LiLi-LOAM	Fail
FAST-LIO2	2.056/3.237
LiDAR/IMU	1.556/3.656
LIU-fusion	**0.668/2.956**

3.4 Runtime Analysis

The evaluation of runtime is performed on an eight-core Intel i7-9700 processor. The aver-age processing time of all sequences is calculated as shown in Table 4. The scan-to-map module dominates the total latency at 23.770 ms, acting as the primary bottleneck for real-time performance. Other modules, such as UWB EKF (0.034 ms), NLOS (0.067 ms), and quality control (0.074 ms), are computationally lightweight, while INS mechanization, factor optimization, and map management contribute moderate overheads. Our algorithm can meet the real-time requirements.

Table 4 AVERAGE TIME OF EACH MODULE

	Time consuming(ms)
NLOS	0.067
Quality control	0.074
UWB EKF	0.034
Scan-to-map	23.770
INS mechanization	1.080
Factor optimization	1.510
Map management	2.303

4 Conclusion

In this paper, we propose a sensor fusion state estimation framework, including NLOS removal, quality control, INS mechanization and LiDAR odometry. Filtering and smoothing optimization solutions have also been applied. Our system is resilient and real-time for complex environments. Experiments demonstrate the robustness, precision and efficiency. Our system can achieve decimeter-level positioning, with improvements of (26.2%, 16.3%, 44.2%) compared with LiDAR/IMU integration in three scenes. And in the NLOS environment, it performs exceptionally well to endure in these challenging environments. In future work, we plan to integrate 3D Gaussian representations [20][21] with our existing framework, aiming to further improve the reliability and precision of localization and mapping, especially under challenging sensing conditions.

References

1. Wu D., Zhong X., Peng X., Hu H., Liu Q. (2022), Multimodal information fusion for high-robustness and low-drift state estimation of ugvs in diverse scenes, IEEE Transactions on Instrumentation and Measurement, Vol. 71, pp. 1-15.
2. Guo H., Zhu J., Chen Y. (2022), E-loam: Lidar odometry and mapping with expanded local structural information, IEEE Transactions on Intelligent Vehicles, Vol. 8, No. 2, pp. 1911-1921.
3. Cheng J., Zhang L., Chen Q., Fu Z., Du L. (2024), High precision and robust vehicle localization algorithm with visual-lidar-imu fusion, IEEE Transactions on Vehicular Technology, Vol. 73, No. 8, pp. 11029-11043.
4. Shahbazian R., Macrina G., Scalzo E., Guerriero F. (2023), Machine learning assists iot localization: A review of current challenges and future trends, Sensors, Vol. 23, No. 7, p. 3551.
5. Jianhua L., Yang Z., Li S., Zlatanova S., Yang B., Li G., Yu B., Zhang Q. (2026), Mmvp: Multi-scene indoor localization for smartphones by using collaborative visual localization and multi-sensor fusion, IEEE Internet of Things Journal.
6. Zhang J., Liu X., Chen S., Tong X., Deng Z., Gu T., Li K. (2024), Toward robust rfid localization via mobile robot, IEEE/ACM Transactions on Networking, Vol. 32, No. 4, pp. 2904-2919.
7. Tang C., Sun W., Zhang X., Zheng J., Sun J., Liu C. (2023), A sequential-multi-decision scheme for wifi localization using vision-based refinement, IEEE Transactions on Mobile Computing, Vol. 23, No. 3, pp. 2321-2336.
8. Liu H., Pan S., Wu P., Yu K., Gao W., Yu B. (2024), Uncertainty-aware uwb/lidar/ins tightly coupled fusion pose estimation via filtering approach, IEEE Sensors Journal, Vol. 24, No. 7, pp. 11113-11126.
9. Xu W., Cai Y., He D., Lin J., Zhang F. (2022), Fast-lio2: Fast direct lidar-inertial odometry, IEEE Transactions on Robotics, Vol. 38, No. 4, pp. 2053-2073.
10. Zou Z., Yuan C., Xu W., Li H., Zhou S., Xue K., Zhang F. (2024), Lta-om: Long-term association lidar–imu odometry and mapping, Journal of Field Robotics, Vol. 41, No. 7, pp. 2455-2474.
11. Bai C., Xiao T., Chen Y., Wang H., Zhang F., Gao X. (2022), Faster-lio: Lightweight tightly coupled lidar-inertial odometry using parallel sparse incremental voxels, IEEE Robotics and Automation Letters, Vol. 7, No. 2, pp. 4861-4868.
12. Shan T., Englot B., Meyers D., Wang W., Ratti C., Rus D. (2020), Lio-sam: Tightly-coupled lidar inertial odometry via smoothing and mapping, Proceedings of 2020 IEEE/RSJ International Conference on Intelligent Robots and Systems (IROS), pp. 5135-5142.
13. Zhong W., Zhang L., Sun Z., Dong M., Zhang M. (2024), Ui-mocap: an integrated uwb-imu circuit enables 3d positioning and enhances imu data transmission, IEEE Transactions on Neural

Systems and Rehabilitation Engineering, Vol. 32, pp. 1034-1044.

14. Ji P., Duan Z., Xu W. (2024), A combined uwb/imu localization method with improved ckf, Sensors, Vol. 24, No. 10, p. 3165.
15. Zheng S., Li Z., Liu Y., Zhang H., Zou X. (2022), An optimization-based uwb-imu fusion framework for ugv, IEEE Sensors Journal, Vol. 22, No. 5, pp. 4369-4377.
16. Nguyen T.H., Xie L. (2023), Relative transformation estimation based on fusion of odometry and uwb ranging data, IEEE Transactions on Robotics, Vol. 39, No. 4, pp. 2861-2877.
17. Li Y., Zou Y., Zhang X., Zang Z., Sun W., Fan J., Lu X., Li X., Liu J. (2024), Lugot: Lidar and uwb fusion for global given object tracking under mobile anchors, IEEE Sensors Journal, Vol. 25, No. 3, pp. 4882-4896.
18. Budiyono A. (2012), Principles of gnss, inertial, and multi-sensor integrated navigation systems, Industrial Robot: An International Journal, Vol. 39, No. 3.
19. Li K., Li M., Hanebeck U.D. (2021), Towards high-performance solid-state-lidar-inertial odometry and mapping, IEEE Robotics and Automation Letters, Vol. 6, No. 3, pp. 5167-5174.
20. Zheng C., Xu W., Zou Z., Hua T., Yuan C., He D., Zhou B., Liu Z., Lin J., Zhu F. (2024), Fast-livo2: Fast, direct lidar–inertial–visual odometry, IEEE Transactions on Robotics, Vol. 41, pp. 326-346.
21. Xiao R., Liu W., Chen Y., Hu L. (2024), Liv-gs: Lidar-vision integration for 3d gaussian splatting slam in outdoor environments, IEEE Robotics and Automation Letters, Vol. 10, No. 1, pp. 421-428.

Authors

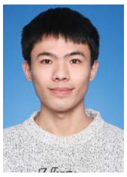

Hong Liu is currently pursuing the Ph.D. degree with the School of Instrument Science and Engineering, Southeast University, Nanjing, China. His current research interests include multisensor fusion, ultra-wideband positioning, and light detection and range (LiDAR) and inertial simultaneous localization and mapping (SLAM).

Shuguo Pan received the Ph.D. degree from Southeast University, Nanjing, China, in 2007. He is currently a vice dean and a professor at the School of Instrument Science and Engineering, Southeast University, Nanjing, China. His research focuses on high-precision positioning, navigation, and timing (PNT) technology and its applications, particularly in the BeiDou Navigation Satellite System.

Wang Gao received the B.S. degree from Southeast University, Nanjing, China, in 2013, and the Ph.D. degree from the same institution in 2018. He is currently an associate professor at the School of Instrument Science and Engineering, Southeast University, Nanjing, China. His current research interest include Vision-LiDAR sensor fusion for positioning in AGV applications.

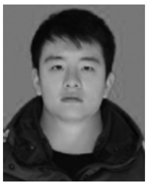

Jinle Xu received the bachelor's degree from the Huazhong University of Science and Technology, Wuhan, China, in 2020. He is currently pursuing the Ph.D. degree with the School of Instrument Science and Engineering, Southeast University, Nanjing, China. His current research interests include unmanned vehicle visual SLAM navigation and positioning and 3-D map positioning reconstruction.

Zhuoxuan Wang received the B.Eng. degree in measuring and controlling technology and instrument from Harbin Engineering University, Harbin, China, in 2021. He is currently working toward the Ph.D. degree in instrumentation science and technology with the School of Instrument Science and Technology, Southeast University, Nanjing, China. His research interests include vehicle model identification and optimization, path planning, and path tracking control.

Feixuan Huang was born in Zhejiang, China, in 2002. He is currently working toward the M.Sc. degree with the School of Instrument Science and Engineering, Southeast University, Nanjing, China. His current research focuses on LiDAR-based global localization for complex environments